Exponential and nonexponential localization of the one-dimensional periodically kicked Rydberg atom

S. Yoshida,[1,2,*] C. O. Reinhold,[1,2] P. Kristöfel,[3] and J. Burgdörfer[1,2,3]

[1]*Department of Physics, University of Tennessee, Knoxville, Tennessee 37996-1200*
[2]*Physics Division, Oak Ridge National Laboratory, Oak Ridge, Tennessee 37831-6373*
[3]*Institute for Theoretical Physics, Vienna University of Technology, A1040 Vienna, Austria*

We investigate the quantum localization of the one-dimensional Rydberg atom subject to a unidirectional periodic train of impulses. For high frequencies of the train the classical system becomes chaotic and leads to fast ionization. By contrast, the quantum system is found to be remarkably stable. We identify for this system the coexistence of different localization mechanisms associated with resonant and nonresonant diffusion. We find for the suppression of nonresonant diffusion an exponential localization whose localization length can be related to the classical dynamics in terms of the ''scars'' of the unstable periodic orbits. We show that the localization length is determined by the energy excursion along the periodic orbits. The suppression of resonant diffusion along the sequence of photonic peaks is found to be nonexponential due to the presence of high harmonics in the driving force.

I. INTRODUCTION

One important motivation for revisiting the issue of classical-quantum correspondence has been the increased appreciation of the apparent contradiction between the ubiquitousness of classical chaotic dynamics and the lack thereof in quantum dynamics. Intense investigations of this field of ''quantum chaos'' (more precisely, of quantum theory of classically chaotic systems) have been stimulated by the experimental realization of simple periodically driven systems that are at the borderline between classical and quantum mechanics. Prototypes of such systems are cooled atoms subject to modulated standing waves [1], Rydberg atoms subject to microwave pulses [2], and Rydberg atoms subject to trains of equispaced half-cycle pulses [3,4].

One of the most interesting discoveries along these lines has been the phenomenon of quantum localization or quantum suppression of classically chaotic diffusion. Quantum localization was first predicted theoretically for the kicked rotor [5]. It was shown that quantum localization can be mapped onto the well-known Anderson localization in solid state physics [6,7]. Subsequently, it was found for Rydberg atoms in microwave fields [8,9] and could be observed as an enhanced quantum stabilization of the atom against ionization. Recently, quantum localization for these systems has been confirmed experimentally [1,2]. Different explanations have been proposed for localization of driven Rydberg electrons employing the concept of the delocalization border [8] and sequential two-level excitations [9]. Mapping of the driven Rydberg atom onto the Anderson localization model is complicated by the fact that, unlike for a kicked rotor, the unperturbed spectrum possesses a cluster point at threshold and a continuous spectrum.

Recently, another driven system involving Rydberg electrons has become accessible: the periodically ''kicked'' Rydberg atom [3,4]. ''Kicks'' denote electric pulses F(t) whose duration T_p is short compared to the unperturbed period of the classical orbital motion, $T_p \ll T_{\mathrm{orb}} = 2\pi n_i^3$, where n_i is the initial level of the atom and atomic units are used throughout this paper. Each pulse transfers a net momentum [10]

$$\Delta \vec{p} = -\int_{-\infty}^{\infty} \vec{F}(t) dt. \qquad (1.1)$$

Thus, a sequence of unidirectional periodic kicks can be approximated by the time-dependent interaction

$$V(t) = -\vec{r} \cdot \Delta \vec{p} \sum_k \delta(t - kT), \qquad (1.2)$$

where T is the period and $\vec{r}$ is the position of the electron. The kicked Rydberg atom differs from a harmonically driven atom in that the dynamics is dominated by the net momentum transfer of the pulse [Eq. (1.1)] or, equivalently, by the presence of an infinite set of high harmonics. As will be discussed below, these features strongly influence the classical and quantum dynamics and lend themselves to an intuitive classical picture of the quantum localization. One of the novel features is that localization involves the (zero-field) continuum, i.e., the positive-energy wave packet remains localized near the nucleus. Moreover, this system is characterized by the simultaneous presence of different localization mechanisms, one of them being the scarring of the wave function near unstable periodic orbits in the chaotic sea.

In Sec. II, we introduce the model of the one-dimensional kicked atom and the methods employed for the solution of the time-dependent Schrödinger equation. Results for the time-dependent excitation spectrum and its localization are presented in Sec. III. The analysis of the suppression of energy diffusion is given in Sec. IV. In Sec. V we discuss the

*Present address: Max Planck Institute for the Physics of Complex Systems, D-01187 Dresden, Germany.

connection between dynamical localization and scars in the quantum phase space distribution.

II. THEORY

The Hamiltonian for the three-dimensional (3D) kicked atom is given by

$$H^{3D}(t) = H_{at}^{3D} + V^{3D}(t) \qquad (2.1)$$

with

$$H_{at}^{3D} = \frac{p^2}{2} - \frac{1}{r}, \quad V^{3D}(t) = -\vec{r} \cdot \Delta\vec{p} \sum_{k=0}^{K-1} \delta(t-kT), \qquad (2.2)$$

where $\vec{p}$ and $\vec{r}$ ar the momentum and position of the electron with respect to the nucleus. The train of δ-shaped kicks is characterized by the total number of kicks K, the kick strength Δp, and the time period between kicks T (i.e., the train frequency $\nu_T = 1/T$). Converged quantum calculations in three dimensions for the long-time evolution of systems with strong coupling to the continuum remain a challenge. We therefore focus in the following on a simplified one-dimensional system for which convergence can be achieved. The latter is crucial for the determination of long-time stability and localization. The 1D system is described by the Hamiltonian

$$H(t) = H_{at} + V(t), \qquad (2.3)$$

$$H_{at} = \frac{p^2}{2} - \frac{1}{q}, \quad V(t) = -q\Delta p \sum_{k=0}^{K-1} \delta(t-kT), \quad (2.4)$$

where $q > 0$ and p are the position and momentum of the electron, respectively. The justification for the approximation of the 3D problem by the 1D model Hamiltonian stems in part from the fact that the classical phase-space structure of this simplified model was found to closely mimic that of the 3D system for initial conditions representing elongated (Stark) orbits [4,18]. This similarity is partly due to the fact that the kicked atom features a global chaotic sea for arbitrarily small Δp. Moreover, for small kick frequencies ν_T where large stable islands exist, classical 3D, classical 1D, and quantum 1D calculations are in good agreement with each other [3]. In the present work, we focus on the quantum dynamics and localization of the 1D model in the high frequency regime $\nu_T \gg \nu_{orb} = 1/(2\pi n_i^3)$, for which the classical system is chaotic. We note, however, that the agreement between the quantum dynamics in 3D and 1D in this regime remains an open question.

Because of the simple δ-shaped perturbation, the classical Hamilton's equations

$$\frac{dq}{dt} = \frac{\partial H(q,p)}{\partial p} = p,$$

$$\frac{dp}{dt} = -\frac{\partial H(q,p)}{\partial q} = -\frac{1}{q^2} + \Delta p \sum_{k=0}^{K-1} \delta(t-kT), \quad (2.5)$$

can be solved by splitting the time evolution into two parts, a kick and a Kepler motion

$$\begin{pmatrix} q_{k+1} \\ p_{k+1} \end{pmatrix} = M_{Coul} \circ M_{kick} \begin{pmatrix} q_k \\ p_k \end{pmatrix}, \qquad (2.6)$$

where q_k, p_k are the position and momentum of the electron just before the kth kick at the time $t_k = (k-1)T - \varepsilon$ ($\varepsilon \to 0$). In this map, the effect of M_{kick} is

$$\begin{pmatrix} q_k \\ p_k + \Delta p \end{pmatrix} = M_{kick} \begin{pmatrix} q_k \\ p_k \end{pmatrix} \qquad (2.7)$$

and the Kepler map M_{Coul} can be obtained numerically solving an implicit analytic equation [4]. The classical survival probability of the atom can be calculated using the classical trajectory Monte Carlo (CTMC) method; i.e., letting a large but finite ensemble of initial conditions evolve in time following Hamilton's equation [Eq. (2.5)], and evaluating the probability for the ensemble to remain in bound states ($H_{at} < 0$). Because of the simplicity of the map, trajectories are numerically stable for long times. In order to mimic the initial quantum Rydberg state, the ensemble of initial conditions are chosen from a microcanonical ensemble with a fixed energy $E_{n_i}^{at} = -1/(2n_i^2)$, corresponding to the principal quantum number n_i.

To simulate the time evolution of the quantum kicked atom, we solve the time-dependent Schrödinger equation (TDSE)

$$i\frac{\partial}{\partial t}|\psi(t)\rangle = H|\psi(t)\rangle, \qquad (2.8)$$

where $|\psi(t)\rangle$ is the wave function of the system. Solutions can be expressed in terms of a time evolution operator, $U(t,0)$, i.e.,

$$|\psi(t)\rangle = U(t,0)|\psi(0)\rangle. \qquad (2.9)$$

Similar to the classical calculation, the time evolution can be split into two parts, i.e., a Kepler motion and a kick corresponding to a free evolution operator $\exp[-iH_{at}T]$, and a boost operator $\exp[iq\Delta p]$, respectively. Thus the time evolution operator can be expressed in terms of the period-one evolution operator $U(T,0)$,

$$U(KT,0) = [U(T,0)]^K \qquad (2.10)$$

which consists of a product of free evolution and boost operators

$$U(T,0) = \exp[-iH_{at}T]\exp[iq\Delta p]. \qquad (2.11)$$

This equation is formally equivalent to the split-operator method. In the present case of δ shaped pulses the split structure is, however, exact rather than an approximation, as it is the case for pulses of finite duration.

The problem is now reduced to the evaluation of matrix elements of these two operators. However, the strong cou-
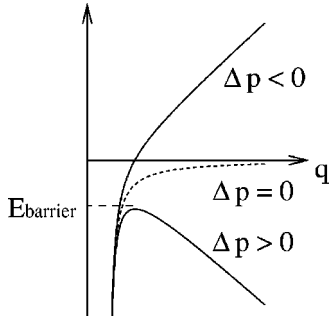
FIG. 1. Potential $V_{\text{Stark}} = -1/q + qF_{\text{av}}$ of the Stark Hamiltonian H_{Stark} for negative ($\Delta p < 0$) and positive ($\Delta p > 0$) kicks.

pling between bound states and the continuum complicates the evaluation of these matrix elements and distinguishes the kicked atom from other systems such as the microwave driven atom. Strong couplings to the continuum can be understood in terms of the Fourier expansion of the interaction

$$V(t) = -\frac{q\Delta p}{T} - \frac{2q\Delta p}{T} \sum_{m=1}^{\infty} \cos(2\pi\nu_m t) \quad (2.12)$$

which contains all harmonics ($\nu_m = m\nu_T$) with equal strength leading to multiphoton coupling to the continuum. Moreover, unlike laser or microwave fields, the average field, $F_{\text{av}} = -\Delta p/T$, is nonzero. Therefore, the Hamiltonian can be rewritten as a sum of a Stark Hamiltonian with a static (dc) field and a dynamic (ac) driving field,

$$H(t) = H_{\text{Stark}} + V'(t) = H_{\text{at}} + qF_{\text{av}} + V'(t) \quad (2.13)$$

$$V'(t) = 2qF_{\text{av}} \sum_{m=1}^{\infty} \cos(2\pi\nu_m t).$$

In the 1D model, the sign of the static field or, equivalently, the direction of the kick plays a crucial role. The spectrum of the H_{Stark} and, consequently, the dynamics of the driven system for different signs of Δp is entirely different: For $\Delta p < 0$ ($F_{\text{av}} > 0$), the quantum spectrum of H_{Stark} is entirely discrete. For $\Delta p > 0$ ($F_{\text{av}} < 0$), the spectrum is entirely continuous and involves a finite number of resonances whose energy levels are below or near the top of the potential barrier $E_{\text{barrier}} = -2\sqrt{\Delta p/T}$ (see Fig. 1). The strength of the ac perturbation and the strength of the dc field in H_{Stark} in Eq. (2.13) are obviously not independent. Therefore, increasing the strength of the Fourier components of the driving field simultaneously steepens the slope of the potential well for $\Delta p < 0$ or lowers the barrier and, hence, reduces the number of below-barrier resonances for $\Delta p > 0$. In both cases, all Fourier components of the kicked system up to infinite order have the same strength. Therefore, all (quasi) bound states of H_{Stark} are strongly coupled to the continuum levels of H_{at} despite the fact that for $\Delta p < 0$, H_{Stark} does not possess a continuous spectrum. This, at first glance, counterintuitive picture suggests the adoption of an alternative description of the time-dependent Hamiltonian in terms of impulsive energy transfers. Calculating the expectation value of the Hamiltonian $\langle H_{\text{at}}\rangle_{k+1} = \langle\psi(t_{k+1})|H_{\text{at}}|\psi(t_{k+1})\rangle$,

$$\langle H_{\text{at}}\rangle_{k+1} = \langle H_{\text{at}}\rangle_k + \langle p\rangle_k \Delta p + \frac{\Delta p^2}{2}. \quad (2.14)$$

This equation expresses the fact that the momentum transfer Δp determines the effective energy transfer and represents the quantum analog to the classical relation

$$H_{\text{at}}(q_{k+1}, p_{k+1}) = H_{\text{at}}(q_k, p_k) + p_k\Delta p + \frac{\Delta p^2}{2}. \quad (2.15)$$

The frequency ν_T which plays a critical role in the description in terms of the harmonic field components [Eq. (2.13)] enters relation (2.14) only in terms of the time interval ($T = 1/\nu_T$) within which the relation is recursively applied to the dynamical system. In the following we will exploit both of these two alternative pictures of the system driven by a field with an infinite set of Fourier components [Eq. (2.13)] and by a sequence of kicks [Eq. (2.14)] in order to understand the suppression of classical chaos and quantum localization. Naturally, Eq. (2.14) will provide the bridge to the classical dynamics while Eq. (2.13) allows us to make contact with the well-studied system of the Rydberg atom driven by a microwave field. For the latter, both studies with an external static field present [2] and without [11] have been performed. The case of a dc field present corresponds to Eq. (2.13) with all high harmonics ($m > 1$) absent while the cases of zero dc field correspond to $F_{\text{av}} = 0$ in H_{Stark} (2.13) in addition to the disappearance of all higher Fourier components above $m = 1$.

The numerical calculations of the quantum evolution require the representation of the period-one evolution operator in a finite Hilbert space P of dimension $N \sim 1500$. We construct an orthonormal basis set from a linear combination of Sturmian pseudostate wave functions [12]

$$\phi_n^S(q) = \frac{2}{n\sqrt{|n_S|}} \frac{q}{n_S} e^{-q/n_S} L_{n-1}^1(2q/n_S), \quad (2.16)$$

where n_S is the so-called Sturmian parameter and L is a Laguerre polynomial. The advantage of using a Sturmian basis set is that small sets of Sturmian wave functions properly describe Coulomb wave functions including bound and continuum states [13].

Because of the strong coupling to the continuum, a finite-basis representation of $U(T,0)$ is not unitary. Unitary approximations for the projections of the unperturbed evolution operator $\exp(-iH_{\text{at}}T)$ and the boost operator $\exp(iq\Delta p)$ onto the P space cannot be applied to the present case of strong coupling to complement Q of the full Hilbert space. These approximations lead to ''reflections'' at the boundary of P causing spurious effects in the numerical calculation of $U(T,0)$. The exact projection should account for the finite outgoing probability flow from P into Q. Both $\exp[-iH_{\text{at}}T]$ and $\exp[iq\Delta p]$ allow transitions to states in the orthogonal complement Q to the subspace P subtended by the basis. Only in the limit that P approximates the whole Hilbert space a finite-basis representation of $U(T,0)$ will approach a unitary matrix.

The nonunitary projection of $\exp[-iH_{at}T]$ and $\exp[iq\Delta p]$ onto P can be evaluated using the so-called repetitive projection method (RPM) [14], which is the equivalent of the masking method in lattice-based basis expansions for atomic pseudostates. In the RPM, the wave function, which initially lives in the P space, is allowed to evolve unitarily into an extended space $P \oplus \delta P \supset P$. Afterwards, the wave function is projected back onto the subspace P, and the probability flux of the wave packet from P to δP ($\delta P \subset Q$) is eliminated. By repeating this procedure, reflections can be suppressed effectively. This applies to both the free evolution operator and the boost operator for small momentum transfers.

For large momentum transfers, an alternative approach is more effective in calculating the projection of $\exp[iq\Delta p]$ onto the P subspace. Namely, the matrix elements of the boost operator

$$\langle \phi_i^S | e^{iq\Delta p} | \phi_j^S \rangle = \int_{-\infty}^{\infty} dq \, \phi_i^S(q) \, e^{iq\Delta p} \, \phi_j^S(q), \quad (2.17)$$

can be expressed analytically by a sum of three hypergeometric functions $_2F_1$ [15]. The evaluation of these functions becomes unstable for large quantum numbers and, in these cases, it is necessary to evaluate Eq. (2.17) using an asymptotic form [16]. The accuracy of the matrix elements was tested by evaluating the $_2F_1$ functions for the typical momentum transfers used in the present work by integer arithmetic.

The point to be noted about our calculations is that the present non-unitary propagation scheme neglects back coupling from the Q space to the P space while suppressing artificial reflections. Part of the reduction of probability is ''physical'' as it corresponds to the elimination of flux from P to Q which would represent ionization and would be irretrievably lost if it were not for artificial reflections. On the other hand, it eliminates also that part of probability flux which would return to P after an intermittent excursion into Q. The latter leads to an underestimate for population probabilities within P. While this error can be considerable for low frequencies ν_T, it is of no importance in the parameter range $\nu_T \gg \nu_{orb}$ where quantum localization occurs. To test the convergence of our calculations, we apply, in addition to the RPM, the stabilization method [13].

For the long-time propagation, we utilize Floquet analysis [17,18] to avoid numerical errors caused by multiplications of large matrices. Floquet states are defined through the eigenvalue equation

$$U(T,0) | \phi_n^F \rangle = e^{-i\mathcal{E}_n T} | \phi_n^F \rangle \quad (2.18)$$

for the period-one evolution operator $U(T,0)$ with quasi-eigenenergies $\mathcal{E}_n = \mathcal{E}_n^R - i\mathcal{E}_n^I$. After K kicks, the propagated wave function becomes

$$| \psi(KT) \rangle = \sum_{n=1}^{N} c_n e^{-\mathcal{E}_n^I KT} e^{-i\mathcal{E}_n^R KT} | \phi_n^F \rangle, \quad (2.19)$$

where c_n are the expansion coefficients of the initial state $|\psi(0)\rangle$ in the basis of Floquet states. The quasieigenenergies
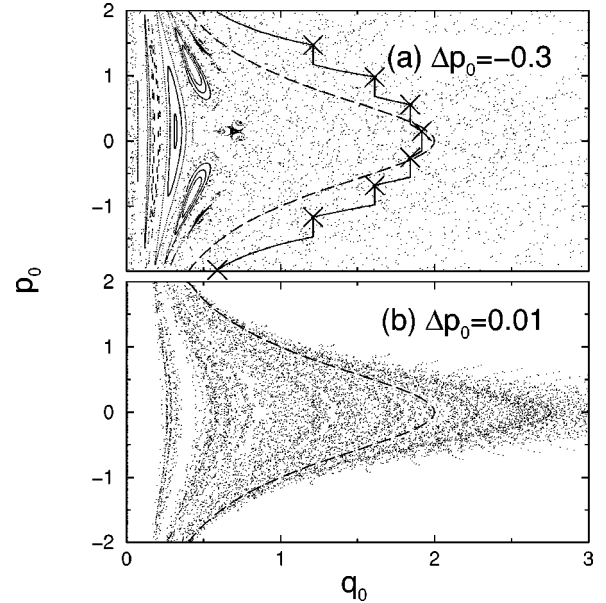

FIG. 2. Poincaré surface of sections for the negatively kicked atom (a) and the positively kicked atom (b) with a scaled frequency $\nu_0 = 16.8$. The black dashed line represents the initial energy level of the system ($-0.5 = p_0^2/2 - 1/q_0$). The thick solid line in (a) is an unstable periodic orbit of the system whose fixed points are denoted by crosses. Periodic orbits for (b) is hardly distinguished from the initial manifold because of the small kick strength.

are, in general, complex ($\mathcal{E}_n^I \geq 0$), which is a direct manifestation of the nonunitarity of the evolution within P (the calculated Floquet states belong to P). An imaginary part $\mathcal{E}_n^I > 0$ describes the decay rate of the Floquet state $|\phi_n^F\rangle$ due to its coupling with Q. Floquet states with $\mathcal{E}_n^I = 0$ remain entirely localized in P or, equivalently, are dynamically decoupled from Q. This property plays a crucial role in the identification and analysis of quantum localization. From Eq. (2.18), we can easily calculate the long-time evolution of the wave function within P. Only those components of the initial state $|\psi(0)\rangle$ that overlap with stable Floquet states $|\phi_n^F\rangle$ with vanishing imaginary part $\mathcal{E}_n^I = 0$ will survive in the limit $K \rightarrow \infty$.

III. CLASSICAL AND QUANTUM EVOLUTION

We present in the following a comparative analysis of the dynamics of the (strongly) negatively ($\Delta p < 0$) and weakly positively ($\Delta p > 0$) kicked Rydberg atom. Negative kicks signify kicks in the direction toward the Coulomb center while positive kicks denote kicks in the direction towards the outer turning point. The reason we focus for positive kicks on weak kick amplitudes is that the classical dynamics is otherwise highly unstable with large Lyapunov exponents such that interesting features of the classical phase space structure are washed out in the quantum wave function.

The classical phase space structure is displayed in Fig. 2 as Poincaré surface of sections from strong negative kicks ($\Delta p = -0.3$) and weak positive kicks ($\Delta p = 0.01$). They correspond to stroboscopic snapshots of the scaled (q_0, p_0)
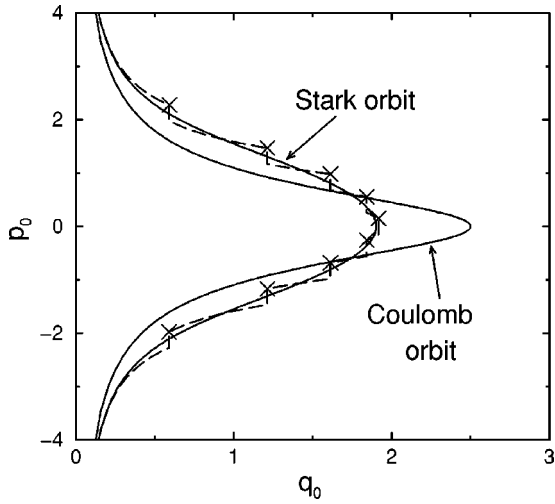
FIG. 3. Comparison of a Stark orbit with scaled energy $E_0^{\text{Stark}} = n_i^2 E^{\text{Stark}} = -2$, a Coulomb orbit with scaled energy $E_0^{\text{at}} = n_i^2 E^{\text{at}} = -0.8$, and an unstable period-$9T$ periodic orbit (dashed line) with its fixed points (crosses). The parameters of the calculation are $\Delta p_0 = -0.3$ and $\nu_0 = 16.8$.

$= (q/n_i^2, pn_i)$ coordinates just before each kick. At a glance, these two Poincaré sections show a large chaotic sea with a completely random pattern. While for negative kicks a few isolated islands of stability remain, the system for positive kicks undergoes a discontinuous transition [19] from regular motion at $\Delta p = 0$ to global hard chaos for arbitrarily small Δp. In this chaotic sea, an infinite number of unstable periodic orbits lie densely, one of which is displayed in Fig. 2.

Periodic orbits are the combination of segments of Kepler orbits ($H_{\text{at}} = $const curves) and kicks (momentum transfer appear as vertical lines). For the Poincaré surface of section, snapshots of the continuous trajectory are taken after every time interval T. As a consequence, periodic orbits appear as a set of fixed points (depicted as crosses in Fig. 2). For stable orbits, they are located at the center of stable islands while for unstable orbits they are immersed in the chaotic sea. These fixed points play an important role when quantum phase space distributions are analyzed.

As discussed in Sec. II, strong unidirectional kicks mimic the presence of a strong dc field [see Eq. (2.13)]. Consequently, the periodic orbit will closely resemble a Stark orbit (i.e., $H_{\text{Stark}} = $const). This is illustrated in Fig. 3 where a Stark orbit is compared with a zero-field ($H_{\text{at}} = $const) Kepler orbit and the sequence of unstable fixed points associated with the impulsively driven Rydberg electron. Note that each smooth segment resembles a Kepler orbit while the combination with the kick renders the entire orbit very similar to a Stark orbit. Obviously, the unstable periodic orbit of the kicked electron closely mimics the unperturbed Coulomb-Stark orbit while the distance to the unperturbed Kepler orbit is large.

In order to present a comparison between the classical and quantum evolution in phase space, we study in Fig. 4 the deformation of the initial torus corresponding to the initial conditions $[H_{\text{at}}(t=0) = E_{n_i}^{\text{at}}]$ under the influence of the first few kicks. As a quantum analog to the classical phase space
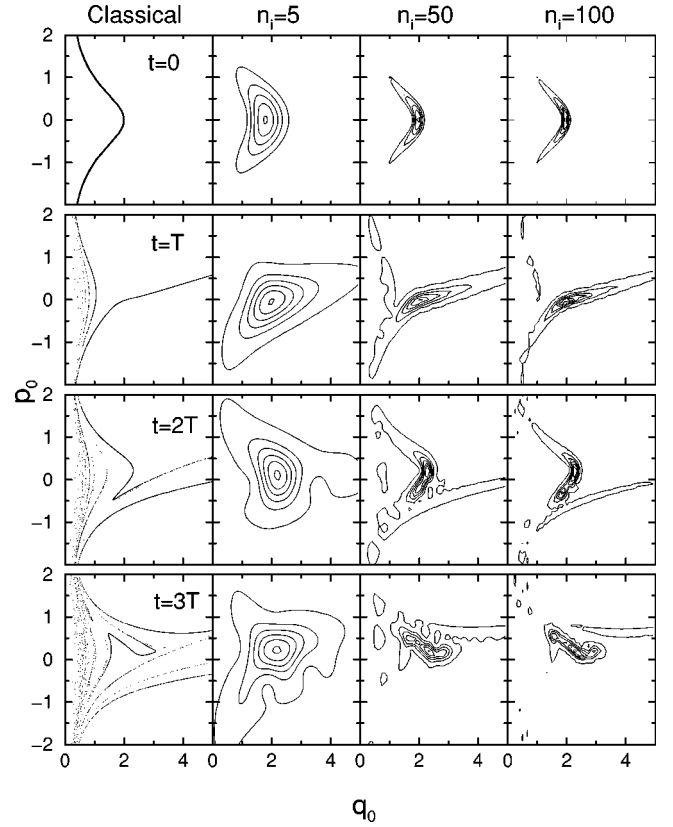

FIG. 4. Initial and time evolved classical and quantum scaled phase space distributions of a 1D hydrogen atom immediately before application of 1,2,3 kicks with a scaled momentum transfer $\Delta p_0 = -0.3$ and a scaled repetition frequency of $\nu_0 = 1.09$. Classical results are represented by an ensemble of 10 000 points and are scaling invariant. Quantum results are plotted for different initial states $n_i = 5,50,100$.

we employ the Husimi distribution [20] defined by

$$P_H(q,p) = \int_{-\infty}^{\infty} dq' \int_{-\infty}^{\infty} dp' P_{q,p}^W(q',p') P_\psi^W(q',p')$$

$$= \frac{1}{2\pi} \left| \int_{-\infty}^{\infty} dr \, \phi_{q,p}^*(r) \psi(r) \right|^2, \quad (3.1)$$

with

$$\phi_{q,p}(r) = (\pi\alpha)^{-1/4} \exp[-(q-r)^2/2\alpha] \exp(ipr), \quad (3.2)$$

where $P_{q,p}^W$ and P_ψ^W are the Wigner distributions of $\phi_{q,p}$ and ψ, respectively. The Wigner distribution is defined as [20]

$$P_\phi^W(q,p) = \frac{1}{\pi} \int_{-\infty}^{\infty} dy \, \phi^*(q+y) \phi(q-y) e^{2ipy}. \quad (3.3)$$

The Husimi distribution is a convolution of the Wigner phase-space distribution with a minimum uncertainty Gaussian wave packet that contains the ''squeezing'' parameter α which can be adjusted to improve the resolution in either q or p. In the present case of Coulomb systems, we use as an
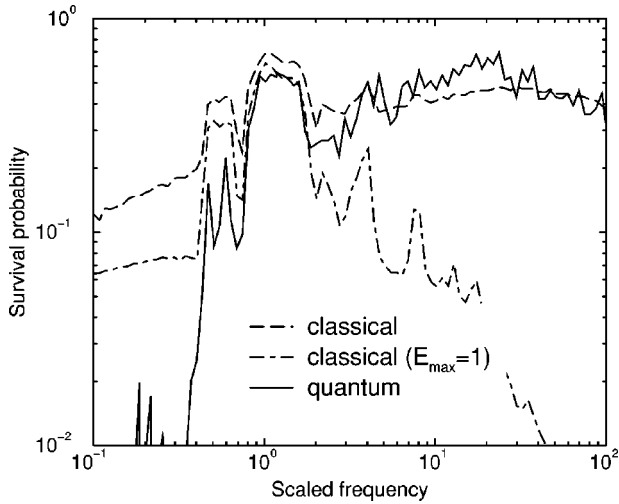
FIG. 5. Survival probability of the kicked 1D hydrogen atom as a function of scaled frequency ν_0 for a fixed scaled momentum transfer $\Delta p_0 = -0.3$ after $K = 200$ kicks. The initial quantum level $n_i = 50$, and the quantum calculations have been performed using a Sturmian parameter $n_S = 60$. See text for the definition of E_{max} in the figure.

FIG. 6. Survival probability as a function of the number of kicks K for three different initial states ($n_i = 5$, 50, and 100). Thick (thin) lines are quantum (classical) results. The parameters for the train of kicks are $\Delta p_0 = -0.3$, $\nu_0 = 16.8$.

optimal choice an n_i-dependent α exploiting the classical scaling invariance. We chose α such that the width of the initial quantum phase space distribution for a given initial state in scaled coordinates is symmetric in both the q_0 and p_0 direction ($\Delta q_0 \sim \Delta p_0$) and converges toward the classical torus as $1/\sqrt{n_i}$. We therefore set

$$\alpha = n_i^3. \tag{3.4}$$

Accordingly, the quantum uncertainty in scaled coordinates is $\Delta p_0 \Delta q_0 = 1/n_i$. Figure 4 displays the evolution of the classical torus and of the Husimi distribution for different n_i as a function of the number of kicks. As the initial torus overlaps with both a stable island and the chaotic sea, the classical evolution displays bending and foliation of the initial torus part of which will be trapped in the center island while the remainder gets scattered in the phase space plane. With increasing n_i, the quantum phase space distribution is increasingly capable of following the classical torus motion. Both the trapping of probability near the stable island as well as the spreading of parts of the wavepacket into the chaotic regime can be recognized.

A suitable quantitative measure for the long-term fate of the wavepacket is its survival probability, i.e., the fraction of the classical as well as quantum phase space probability which remains bound (i.e., with energies $E^{at} < 0$). The survival probability serves as a hallmark for the absence or suppression of chaotic motion since the latter leads inevitably to ionization as $K \rightarrow \infty$ due to the strong coupling to the continuum. Fig. 5 displays the survival probability of the kicked atom after $K = 200$ impulses as a function of scaled frequency $\nu_0 = \nu_T / \nu_{orb}$ of the train of pulses. The initial state is $n_i = 50$ and the scaled momentum transfer $\Delta p_0 = -0.3$ is chosen such that the classical phase space for this system contains sizeable stable islands (e.g., Fig. 2). For scaled fre-
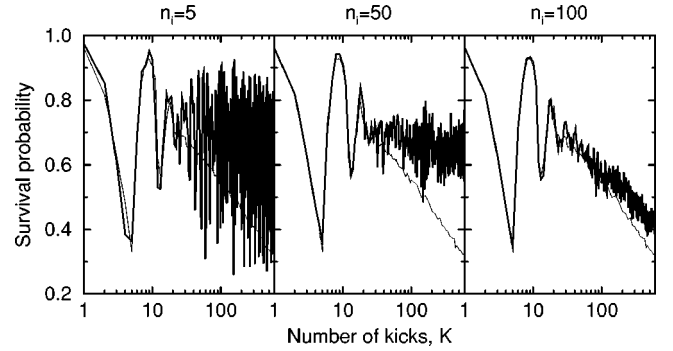
quencies, $\nu_0 \sim 1$, pronounced peaks are observed in both the classical and quantum calculations. The enhanced stability against ionization near $\nu_0 \sim 1$ is due to the presence of a large classical island of stability near the initial torus. This island is also evident in quantum Floquet states with zero imaginary part of the quasieigenenergy [18]. Stable Floquet states $\mathcal{E}^I = 0$ that are in direct correspondence to classically regular motion on intact tori are referred as stabilization in contradiction to quantum localization for which stable Floquet states with $\mathcal{E}^I = 0$ do not have a classically stable counterpart but are associated with classically chaotic motion.

Near $\nu_0 = 1$ and below, the quantum survival probability underestimates the classical probability. This is due to the nonunitary time evolution associated with the RPM. Quantum trajectories that intermittently leave the P space and enter Q space are eliminated by the projection before returning to P space. The effect of the elimination by projection due to a limited basis size can be simulated in classical simulations discarding trajectories that leave a certain region of phase space. As an example, we show in Fig. 5 such a classical projection in which we have eliminated all trajectories that intermittently reach a scaled energy $E_{max} = E^{at} n_i^2 > 1$. This simulation agrees, indeed, much better with the quantum survival for $\nu_0 \lesssim 3$ and confirms that the discrepancy between classical and quantum survival is not an indication of the breakdown of classical-quantum correspondence but an effect of the limited basis size, i.e., of the nonconvergence of the quantum calculations. For higher frequencies $\nu_0 > 3$, however, the quantum survival probability is as high or exceeds the classical one and is found to be converged as detailed tests using the stabilization method [13] confirm. This is the regime of quantum localization whose analysis is at the center of the remainder of this paper.

Examples of localization for $\nu_0 = 16.8$ are shown in Fig. 6 for $\Delta p_0 = -0.3$ and Fig. 7 for $\Delta p_0 = 0.01$. In both cases, the initial torus lies in the completely chaotic region of phase space [Figs. 2(a) and 2(b)] far from any stable island. Figure 6 shows the time evolution of the survival probability $P_{sur}(H_{at} < 0)$ whereas Fig. 7 displays the recurrence probability $P_{rec}(n_i) = |\langle n_i | \psi(t) \rangle|^2$ as a function of time. The classical analog to P_{rec} is defined as
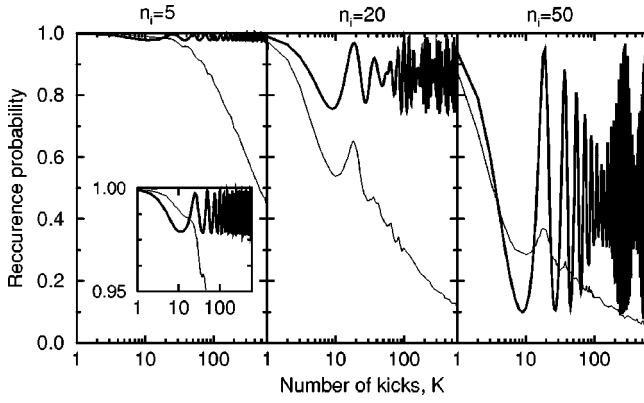
FIG. 7. Recurrence probability of the positively kicked atom with $\Delta p_0 = 0.01$ and $\nu_0 = 16.8$ for different initial levels $n_i = 5, 20, 50$. Thick (thin) lines are quantum (classical) results.

$$P_{\text{rec}}^{\text{cl}}(t) = \int_{E_{n_i}^{\text{at}} - \Delta_{n_i} < H_{\text{at}} < E_{n_i}^{\text{at}} + \Delta_{n_i+1}} dq \, dp \, dE \, f(q,p,t),$$

(3.5)

where $f(q,p,t)$ is the classical probability density in phase space, $E_{n_i}^{\text{at}} = -1/2n_i^2$, and $\Delta_{n_i} = 1/4(n_i-1)^2 - 1/4n_i^2$. Note that the classical recurrence probability is not exactly classically scaling invariant because the quantum energy level spacing is taken into account in Eq. (3.5). For positive kicks, the survival probability is a structureless function since electrons are irretrievably lost once ionized since subsequent kicks in outbound directions lead only to further acceleration and energy gain and precludes any recapture. Therefore, non-monotonic structures appear only in the recurrence probability which are due to redistribution among bound states. Both the quantum survival probability for negative kicks (Fig. 6) and the quantum recurrence probability for positive kicks (Fig. 7) display pronounced oscillations which initially closely follow the classical predictions before completely departing from each other after about $K \simeq 30$ kicks. Obviously, the oscillation frequency is classical in origin, even though the classical phase space distribution can follow the oscillatory pattern only for a limited time before the probability quickly decays. The correspondence between the classical and quantum evolution is maintained for longer time periods (or number of kicks K) as n_i increases, i.e., as we approach the semiclassical limit.

IV. SUPPRESSION OF DIFFUSION

In the previous section, an increased quantum survival probability relative to the classical survival probability for initial conditions in a region of the classically chaotic phase space was found. This can be understood as a hallmark of quantum localization. One of its characteristic features is the suppression of diffusion in energy space for time-dependent systems. We therefore study now the spectral distribution $\rho_K(E)$ after K kicks where $E = E^{\text{at}}$ or $E = E^{\text{Stark}}$ represents the expectation value of H_{at} or H_{Stark}, respectively. Within a discrete basis, the spectral density is given by
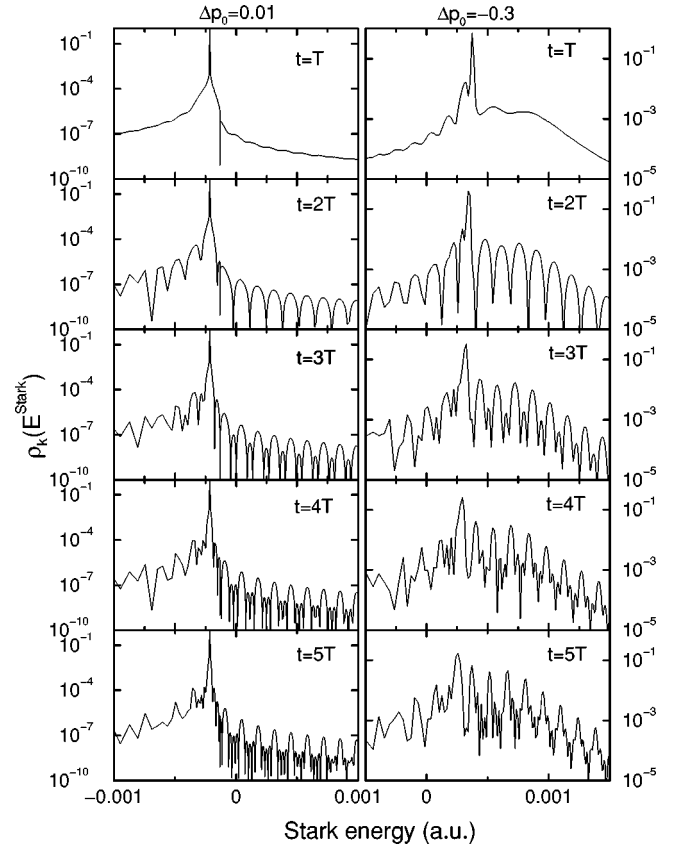

FIG. 8. Time evolution of the Stark energy distribution $\rho_K(E^{\text{Stark}})$ for $\nu_0 = 16.8$ and different strengths of the kicks, $\Delta p_0 = 0.01$ (left column); $\Delta p_0 = -0.3$ (right column). The initial state of the atom is prepared in a Stark state which has the largest overlap with the hydrogenic $n_i = 50$ level.

$$\rho_K(E) = |d_n(KT)|^2,$$

(4.1)

where d_n is the expansion coefficient of the time-evolved wave function in the basis of time-independent eigenstates $|\chi_n\rangle$ of either H_{at} or H_{Stark} with eigenenergies $E_n^{\text{at (Stark)}}$,

$$|\psi(KT)\rangle = \sum_n^N d_n(KT)|\chi_n\rangle.$$

(4.2)

Figure 8 displays the short-time evolution of the spectral density of H_{Stark} for the first five negative and positive kicks. After one kick, the spectral distribution mimics the transition strength due to the kick, i.e., the inelastic form factor. It is strongly peaked near the initial state and falls off with an inverse power-law dependence for large $|E^{\text{Stark}} - E_{n_i}^{\text{Stark}}|$ where $E_{n_i}^{\text{Stark}}$ is the initial Stark energy. The sharp dip for positive kicks is due to the fact that some of the near-threshold resonances are localized in the outer well rather than in the inner well (see Fig. 1), having therefore an exponentially small overlap with the initial state. With increasing number of kicks, the spectral distribution builds up oscillating components. It is the build-up of (destructive) interferences that ultimately suppresses further spread and diffusion in energy space and "freezes" out the energy distribution of
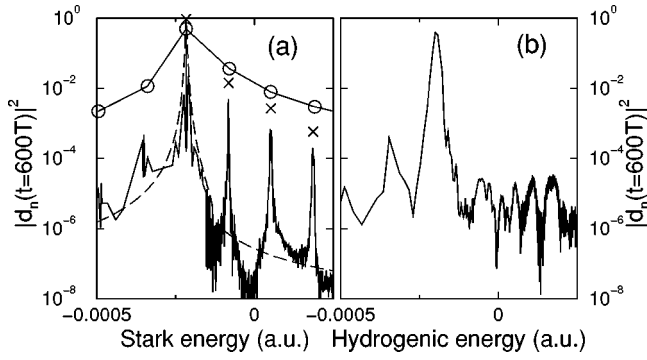
FIG. 9. Energy distributions of the final state of the atom after application of 600 positive kicks with $\nu_0 = 16.8$ and $\Delta p_0 = 0.01$. (a) The atom is initially prepared in the Stark state $|\chi_{n_i}^{\text{Stark}}\rangle$ with the largest overlap with the $n_i = 50$ hydrogenic level. The crosses are the time-averaged integrated probabilities of the resonant peaks. The solid lines with circles are the average excitation probabilities given by $P_{0 \to m}^{m\omega}$ such that the adjacent energy difference between circles is equal to ω. The dashed line is the dipole coupling strength $|\langle \chi_n^{\text{Stark}} | q | \chi_{n_i}^{\text{Stark}} \rangle|^2$ in arbitrary units. (b) Same as (a) but for a hydrogenic initial state in $n_i = 50$ and as a function of hydrogenic energy.

the wave packet. Figures 9 and 10 show ''frozen'' quasistationary energy distributions after 600 kicks for different kick strengths. Obviously, the localized energy distribution possesses a variety of intricate features which can reveal different underlying localization mechanisms. In the following we analyze these features in detail and we distinguish between suppression of resonant and nonresonant diffusion.

A. Suppression of nonresonant diffusion

In general, the suppression of classically chaotic nonresonant diffusion is associated with the discreteness of quasi-eigenenergy levels in quantum mechanics. Fishman et al. [7,21] have provided an explanation of this suppression for the kicked rotor

$$H_{\text{rot}} = 2p_\theta^2 + K_{\text{rot}} \cos \theta \sum_k \delta(t-k) \qquad (4.3)$$
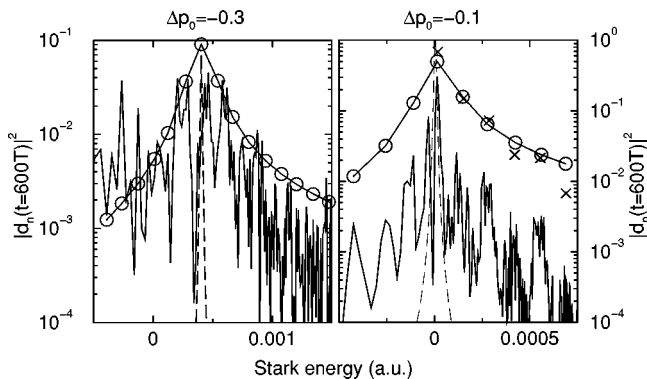

FIG. 10. Same as Fig. 9(a) but with momentum transfers $\Delta p_0 = -0.3$ (left) and -0.1 (right).

by mathematically reducing it to the ''tight-binding'' Anderson model. Note that this Hamiltonian is scaled in the units of the inertia of rotor I and the time interval between kicks T. The key point is that in this model, all the Floquet states $|\varphi_{\mathcal{E}}^F\rangle$ with quasienergies $\mathcal{E}$ become exponentially localized around some momentum p_θ with the same localization length Δ_L,

$$\langle l | \varphi_{\mathcal{E}}^F \rangle \sim \exp\left(-\frac{\tilde{\hbar} |l - l_{\mathcal{E}}|}{\Delta_L} \right). \qquad (4.4)$$

where $\tilde{\hbar} = \hbar T/I$ is a scaled Planck constant, and p_θ is quantized and takes values $p_\theta = l\tilde{\hbar}$, $(l = 0, \pm 1, \pm 2, \dots)$. Floquet states with nearly identical quasienergies are generally localized around centers which are far apart. On the other hand, two Floquet states localized at centers close compared to Δ_L have a quasienergy separated by the spacing proportional to Δ_L^{-1} [7].

If, for simplicity, we start with a well-localized state, $\langle l | \psi(t=0) \rangle = \delta_{l l_{\text{ini}}}$, only Floquet states whose centers $l_{\mathcal{E}}$ are within a momentum range Δ_L of the initial level l_{ini} contribute to the time evolution. Hence, the expectation value of $(p_\theta - l_{\text{ini}})^2$ cannot become much larger than Δ_L^2. The effective number of Floquet states contributing to the time evolution is Δ_L. Since quasienergies $\mathcal{E}$ (more precisely, $\mathcal{E}T$) are distributed over the interval $\{0, 2\pi\}$ (note that $T = 1$ in the present units), the typical energy space becomes $\delta\mathcal{E} \sim 2\pi/(\Delta_L T)$. Momentum (and energy) diffusion continues up to a time t^* where the time-energy uncertainty allows the resolution of the discrete Floquet spectrum

$$t^* \approx 2\pi/\delta\mathcal{E} \simeq \Delta_L. \qquad (4.5)$$

t^* is usually referred to as the break time. In the classical limit, i.e., $\hbar \to 0$, the time evolution involves an infinite number of Floquet states and the recurrence of the system never happens, i.e., $t^* \to \infty$.

Some of these properties previously observed for the kicked rotor can be identified in the present case of the periodically kicked Rydberg atom. Specifically, the dominant Floquet states $|\phi_n^F\rangle$ overlapping with the initial state [i.e., large $|c_n|$ values in Eq. (2.19)] and governing the time evolution are found to be exponentially localized in *state number space* (see Fig. 11). The latter specification is crucial in identifying the value of the localization length in the present case since the relation between state number $|\chi_n\rangle$ (ordered with increasing energy E_n) and energy is complicated. If $E_n = E_n^{\text{at}}$ are taken to be the eigenvalues of H_{at}, the spectrum is characterized by the presence of a spectral cluster point at the ionization threshold of H_{at} and a (discretized) continuum above. If $E_n = E_n^{\text{Stark}}$ correspond to the eigenvalues of H_{Stark}, the relation between state number and E_n is clear for $\Delta p < 0$ since the spectrum is discrete. However, for $\Delta p > 0$ the spectrum is continuous and a discrete representation is obtained only when using a finite basis set. We will, therefore, in the following inquire about the localization in energy space including the continuum energy spectrum. The state number in Fig. 11 corresponds to the spectrum of H_{at} and involves only bound states.
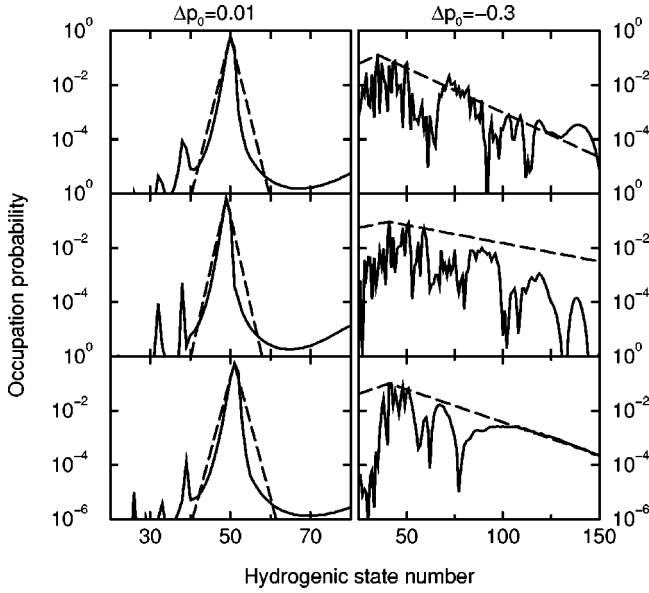
FIG. 11. Probability distribution of three dominant Floquet states in state number space of H_{at} for different kick strengths, left column: $\Delta p_0 = 0.01$, right: $\Delta p_0 = -0.3$. The dashed lines correspond to $\exp[-|n - n_i|/\Delta_L]$ with Δ_L estimated from the state entropy.

Figure 11 shows that the localization length of Floquet states in state number space can be determined from

$$\Delta_L^n = \frac{1}{2} e^{S_n}, \tag{4.6}$$

where S_n is the state entropy [22] of the Floquet state $|\phi_n^F\rangle$ and is given by

$$S_n = -\sum_{l=1}^{N} p_l^n \ln p_l^n \tag{4.7}$$

and $p_l^n = |\langle \chi_l | \phi_n^F \rangle|^2$. Different Floquet states contributing significantly to the time evolution have very similar values for Δ_L^n indicating the approximate ''universality'' of the localization length similar to that for the kicked rotor.

One consequence of the localization description in terms of Floquet states with centers close to each other on a scale of Δ_L is that their quasieigenenergies should display ''level repulsion.'' That is, if the quasieigenenergies are depicted as a function of any of the parameters of the perturbation (either ν_T or Δp), they exhibit pronounced avoided crossings, pointing to ''strong couplings'' among them. As a result, spectral statistics for the nearest-neighbor spacing of the real part of $\mathcal{E}^F$, should display a Wigner-like behavior or, more generally, a Brody distribution [23] of the form

$$P_{\text{Brody}}(D) = AD^{1+b} \exp(-BD^{1+b}), \tag{4.8}$$

where $A = (1+b)B, B = [\Gamma((2+b)/(1+b))]^{1+b}$, $D = \Delta\epsilon/\langle\Delta\epsilon\rangle$ is the scaled nearest-neighbor spacing and b is the Brody parameter.

A Wigner distribution corresponds to the limit $b \to 1$ while a random Poisson distribution results from $b \to 0$. De-
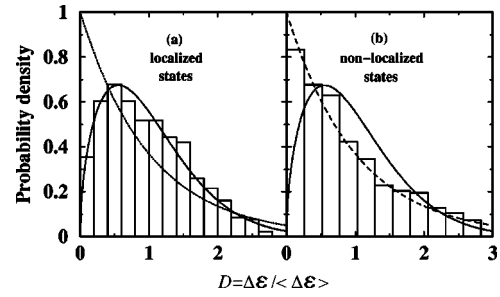

FIG. 12. Comparison of calculated scaled nearest neighbor energy spacing statistics (bars) with Poisson distributions (dashed lines) and best fit Brody distributions with $b = 0.527$ (solid lines). The two figures consider (a) 465 localized states with $|e^{-\mathcal{E}^I T}| > 0.99$ and (b) 919 nonlocalized states.

lineation of the spectral statistics in this system is complicated by the fact that quasieigenenergies $(\mathcal{E}T)$ are defined by only modulo 2π. Therefore, Floquet states living in different regions of phase space can have, coincidentally, close-lying quasieigenvalues. At the same time, the value of the imaginary part allows to identify the localized and delocalized character of the Floquet states. As criteria for selecting the subset of Floquet states involved in the quantum localization with localization length Δ_L we use the proximity to the unit circle $e^{-T\mathcal{E}^I} \geq 0.99$. Figure 12(a) displays the nearest-neighbor spacing distribution of 465 localized Floquet states for an initial state with $n_i = 100$, $\nu_0 = 16.8$ and strong negative kicks. For comparison, Fig. 12(b) shows the nearest-neighbor spacings for quasienergy eigenvalues for nonlocalized states. Obviously, the transition from localized to delocalized Floquet states is accompanied by a transition from a Brody distribution to a Poisson distribution. The fact that the Brody parameter reaches for localized states only about $b \approx 0.53$ rather than unity appears to indicate that the statistical ensemble may contain states localized in different areas in phase space which show some accidental near degeneracies.

B. Suppression of resonant diffusion

The complex structure of the localized energy spectrum in Figs. 9 and 10 indicates that other localization mechanisms are simultaneously present. One of them is the suppression of resonant diffusion.

When a frequency of the perturbation matches the energy difference between two levels, the transition probability becomes resonantly enhanced. Sequences of resonant transitions can lead the diffusion in energy space. However, the nonlinear behavior of energy levels (e.g., $E \sim n^{-2}$) leads to dephasing and suppresses resonant diffusion. A simple picture along these lines based on a two-state model was introduced by Jensen et al. [9] to explain quantum localization for the Rydberg atom driven by a weak microwave field. The basic idea is that excitation occurs predominantly between resonant energy levels separated by the one-photon energy ω, where $\omega = 2\pi\nu$ is the angular frequency of the perturbation. However, since quantum energy levels of the atom are discrete and their level spacing is not equidistant, the atom is

excited to energy levels which are nearby the resonant energy levels. This quantum ''detuning'' suppresses the resonant excitation process and causes the quantum localization.

Assuming that the quantum detuning is randomly distributed around the resonant energy and in an interval given by the adjacent level spacing around the excited state δE_1, the average quasiresonant excitation induced by a single harmonic with frequency ω from a state $|0\rangle$ to a state $|1\rangle$, is given by [9]

$$P_{0\to 1}^{\omega}=\frac{|F_{av}\langle 0|q|1\rangle|}{\delta E_1}\tan^{-1}\left[\frac{\delta E_1}{2|F_{av}\langle 0|q|1\rangle|}\right]. \quad (4.9)$$

For Rydberg atoms in a microwave field, this probability defines the localization length since it approximately acquires the same numerical value for different energy levels (e.g., $P_{0\to 1}^{\omega}\sim P_{i\to i+1}^{\omega}$). Thus, the final energy distribution $\rho(E)$ for that problem becomes exponentially localized in energy space, i.e.,

$$\rho(E)\sim\exp\left(-2\frac{|E-E_i|}{\omega L_{\text{loc}}}\right), \quad (4.10)$$

where E_i is the initial energy and L_{loc} is the localization length defined by

$$L_{\text{loc}}=-2/\ln P_{0\to 1}^{\omega}. \quad (4.11)$$

For the microwave problem both the suppression of resonant as well as nonresonant diffusion has been interpreted as strong (or Anderson-type) localization since they both result in an exponential distribution, however, not necessarily on the same scale (energy or state number). For the kicked atom, these mechanisms are vastly different and can be easily distinguished from each other. The origin lies in the frequency distribution of the periodic perturbation.

The kicked atom is equivalent to the system of an atom in a dc field perturbed by a superposition of all higher harmonics (Eq. 2.13). Each harmonic term $\cos(2\pi m\nu t)$ induces resonant excitation from $|0\rangle$ to $|m\rangle$ ($m=1,2,\dots$). When this direct excitation becomes significant compared to the successive resonant excitation, $|0\rangle\to|1\rangle\to\cdots\to|m\rangle$, the energy distribution is not exponentially localized. This ''multiphoton'' transition corresponds to large energy changes compared to the nearest-neighbor spacing. Therefore, exponential localization in state number space and energy space are, in general, different. Moreover, localization includes here the positive-energy spectrum. Direct excitation by a multiphoton transition with frequency $m\omega$, averaged over the detuning δE_n, the excitation probability is given by

$$P_{0\to m}^{m\omega}=\frac{|F_{av}\langle m|q|0\rangle|}{\delta E_m}\tan^{-1}\left[\frac{\delta E_m}{2|F_{av}\langle m|q|0\rangle|}\right] \quad (4.12)$$

where $\langle m|q|0\rangle$ is the dipole coupling from $|0\rangle$ to $|m\rangle$. In the present problem, direct excitation dominates over sequential excitation, $P_{0\to m}^{m\omega}>\Pi_{i=0}^{m-1}P_{i\to i+1}^{\omega}$. This is confirmed by the fact that the resonant peak structure appears even after two kicks, which is much shorter than the time for which significant successive transitions from $|0\rangle$ to $|m\rangle$ levels are expected (Fig. 8). The arguments leading up to the localization length [Eq. (4.11)] no longer apply to this case and, consequently, we observe a nonexponential localization in energy space (Fig. 9). Moreover, the variation of the peak heights of the multiphoton peaks $m\omega$ closely mimic the behavior of the dipole coupling strength, also displayed in Fig. 9. In fact, the time-averaged integrated peaks agree quite well with the direct excitation probabilities $P_{0\to m}^{m\omega}$ [Eq. (4.12)].

This nonexponential energy localization is well separated and clearly distinguishable from the nonresonant diffusion which determines the width of each of the photonic peaks for small kick amplitudes ($\Delta p_0=0.01$). The spectral density [Eq. (4.1)] is clearly dependent on the choice of the basis. Because of the alternate choice of a time-dependent Hamiltonian, the expansion of the time-dependent wave function can be performed in terms of eigenstates within the zero-field Hamiltonian or the Stark Hamiltonian. The spectral distribution [Eq. (4.1)] displays the photonic peak structure which is more pronounced in the Stark basis (Fig. 9).

Since for small kick strengths two processes of diffusion are observed in the kicked atom, two localization lengths are defined, one for each diffusion; the localization length within the dominant peak (nonresonant diffusion) and the one involving all resonant peaks (resonant diffusion). Since nonresonant diffusion is the result of the transition to the neighboring energy levels, the dipole coupling $\langle\chi_n^{\text{Stark}}|q|\chi_{n_i}^{\text{Stark}}\rangle$ controls the localization length within a peak (shown in dashed lines Fig. 9). As discussed above, the shape of the dipole coupling controls the height of subsequent photonic peaks. Therefore, in the case of small positive kicks, the dipole coupling strength governs both the exponential localization length for nonresonant diffusion as well as the nonexponential localization for photonic peaks in the positive-energy continuum.

In the case of strong kicks ($\Delta p_0=-0.1,-0.3$, Fig. 10) the width of each photonic peak is broadened such that adjacent photonic peaks begin to overlap. Therefore, the resonant peaks merge and well defined structures are destroyed. Moreover, an additional quasiregular pattern with an energy spacing that is smaller than the resonant spacing appears. This feature will be analyzed in more detail below. Nevertheless, the presence of two competing localization mechanisms is still evident. The localization length as defined through the state entropy characterizes the width of the sharp peak near the initial state. Similarly, the decay of the more distant peaks follows the nonexponential decay pattern of the photonic peaks. However, due to the presence of an infinite set of harmonics the peak heights do not become stationary but oscillate. It is therefore necessary to introduce some form of time averaging to measure the localization length of the system. We therefore take the time average over a period of the oscillation.

V. LOCALIZATION AND SCARS

We analyze now in more detail the additional rapidly varying structures in the spectral distribution seen in Fig. 10. They provide a key to a classical interpretation of the localization that suppresses nonresonant diffusion and its localiza-
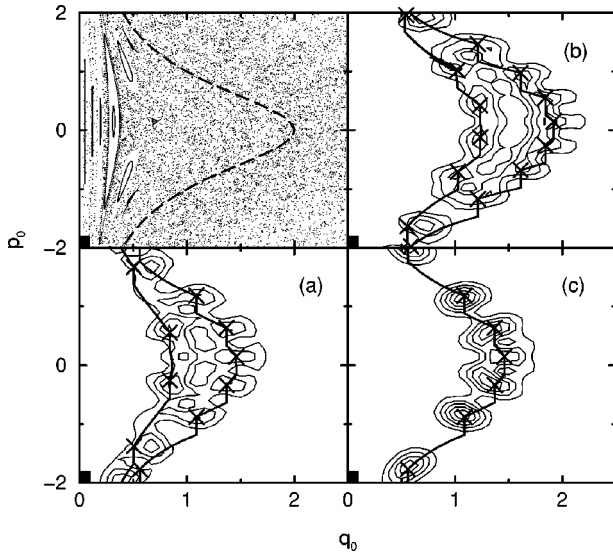
FIG. 13. Poincaré surface of section and Husimi distributions of three dominant Floquet states for the kicked $n_i=50$ atom with $\Delta p_0=-0.3$ and $\nu_0=16.8$. The figures are ordered according to the importance of the Floquet states in the time evolution. The dashed line in the surface of section represents the initial energy level of the system. The thick solid lines are unstable periodic orbits of the system whose fixed points are denoted by crosses.

tion length. To this end, we determine the Husimi distribution of the dominant Floquet states that carry the strongest weight of the localized wave packet. These are Floquet states with vanishing imaginary part. Figure 13 displays the quantum phase space distribution of the leading Floquet states for strong negative kicks. Remarkably, they are strongly localized around unstable periodic orbits.

In analogy to scars of wave functions for time-independent states [24] these structures can be identified as scars in the quantum phase space in time-dependent systems. The important point to be noted is that unstable periodic orbits have measure zero in the classical phase space and therefore do not leave a trace in the classical phase space portrait, the Poincaré surface of section (Fig. 2). Only quantum dynamics (or the finite value of $\hbar$) adds some ''flesh'' to the skeleton of classical dynamics such that unstable periodic orbits become the carrier of a significant fraction of the localized probability density.

While a Floquet state itself is stationary, its correspondence to a classical periodic orbit allows for an intuitive time-dependent interpretation given by the motion of the electron along the periodic orbit. Each kick transports the electron to a different energy hypersurface. After a certain number of kicks (i.e., the period of the unstable periodic orbit) the electron returns to its initial location. For example in Fig. 14 the electron is initially near the outer turning point of the orbit at $p_0\sim0,q_0\sim2$ and acquires a negative average momentum. Each kick on the inbound motion speeds up the electron and excites it to a higher energy level including the hydrogenic continuum. Eventually, the electron scatters at the nucleus, turns around, and acquires a positive momentum. Subsequently, each kick during the outbound part of the trajectory slows down the electron deexciting it to a lower
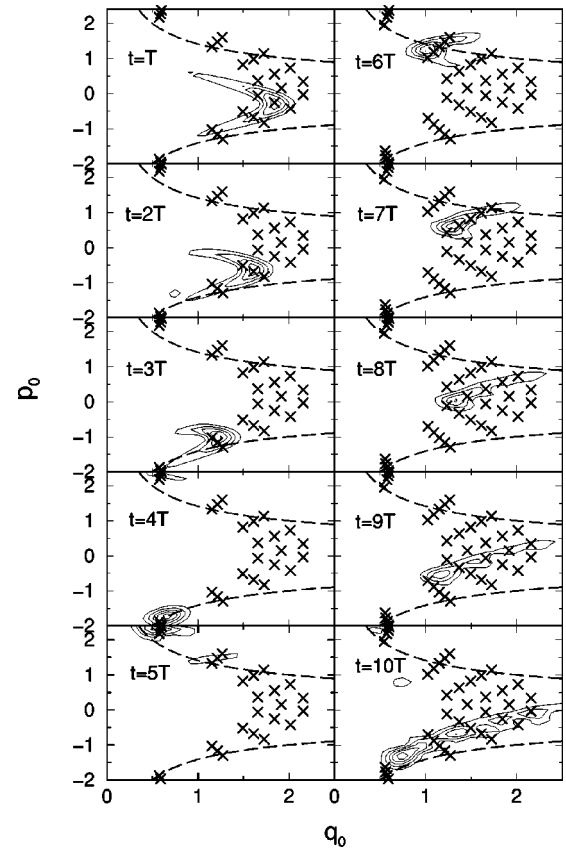

FIG. 14. Time evolution of the Husimi distribution of a hydrogenic $n_i=50$ state subject to a train of kicks with $\Delta p_0=-0.3$ and $\nu_0=16.8$. The crosses represent fixed points of periodic orbits with period $8T$, $9T$, and $10T$ (on the right column, those with period $6T$ and $7T$ are added). The dashed line represents the ionization threshold.

energy level and becoming a bound hydrogenic state once again. Since several Floquet states with different quasienergies $\mathcal{E}^R$ contribute to the time evolution, the entire wave function, which is a coherent superposition of ''stationary'' Floquet states, has a relative time evolution phase, exp $[-i(\mathcal{E}_n^R-\mathcal{E}_m^R)T]$, and resulting in the motion of the wavepacket as seen in Fig. 14. For example, the period-$9T$ motion of the quantum wave packet is generated by the relative phase with $(\mathcal{E}_n^R-\mathcal{E}_m^R)\sim 2\pi k/9T$, where k is an integer. After the period $9T$, the relative phase becomes $\exp[-i(\mathcal{E}_n^R-\mathcal{E}_m^R)9T]\sim\exp(-i2\pi k)$ and comes back to the original phase. Thus, this pair of Floquet states contribute to the quantum time evolution with a period $9T$. In the case of Fig. 14, the level spacing distribution among the dominant Floquet states shows the peaks around $2\pi k/9T$. This is the reason why the time evolution of the survival probability (Fig. 6) is dominated by the period $9T$ oscillation. Note that three out of nine fixed points lie at positive energies ($H_{at}>0$). The motion along a classical unstable periodic orbit immediately explains the oscillation in the classical survival probability in Fig. 6.

The paradoxical fact is, at first glance, that the motion of the quantum wave packet is obviously stable while the underlying classical trajectories are not. The stabilization is ob-
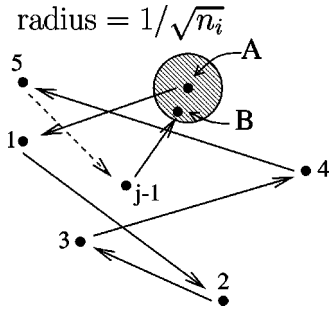
FIG. 15. Schematic picture of the build-up of scars of a classically unstable orbit in the quantum phase space distribution due to the finite quantum resolution (shaded area). The arrows illustrate a trajectory staring in A and ending in B at a distance from A which cannot be resolved.

viously the consequence of the finiteness of $\hbar$. The following simple picture (Fig. 15) explains the essence of this mechanism. Consider a wave packet that is localized in both scaled q or p coordinates to within

$$\Delta p_0^{\text{qm}} = \Delta q_0^{\text{qm}} = \hbar^{1/2} \simeq n_i^{-1/2} \qquad (5.1)$$

given by the quantum uncertainty in scaled coordinates. Close to unstable periodic orbits, classical trajectories separate from each other during one period by

$$r_0^{\text{cl}}(T_{\text{PO}}) = r_0^{\text{cl}}(0) \, e^{\chi_{\text{PO}}}, \qquad (5.2)$$

where $r_0^{\text{cl}}(t) = \sqrt{(\Delta q_0^{\text{cl}}(t))^2 + (\Delta p_0^{\text{cl}}(t))^2}$, and $\chi_{\text{PO}} = \lambda_{\text{PO}} T_{\text{PO}}$ is the stability index of the orbit, and λ_{PO} and T_{PO} are the Lyapunov exponent and period of the periodic orbit, respectively. If now the trajectory after one period returns to the initial condition to within a distance of the order of the quantum uncertainty ($\sim 1/\sqrt{n_i}$), the classical spread of the trajectory does not suffice to effectively disperse the quantum wave packet. As a result, the quantum wave packet can retrace its trajectory and a build-up of density due to the constructive interference along the path becomes possible (Fig. 15). Combining Eqs. (5.1) and (5.2) leads to the estimate for quantum localization to occur

$$r_0^{\text{cl}}(0) \, e^{\chi_{\text{PO}}} \lesssim \frac{1}{\sqrt{n_i}}, \qquad (5.3)$$

where the width $r_0^{\text{cl}}(0)$ is given by the size of the region within which the linearization including the calculation of the monodromy matrix and the stability index remains valid. As a rough estimate one can take a distance small compared to the distance between adjacent fixed points along the periodic orbit. This quantity is given by classical dynamics independent of the quantum number (or $\hbar$). One consequence of Eq. (5.3) is that any weakly unstable orbit with $\chi_{\text{PO}} \gtrsim 0$ will be efficient in carrying probability density for quantum localization. As $n_i \to \infty$ (or $\hbar \to 0$), the scars along unstable periodic orbits will disappear, the larger χ_{PO} the smaller n_i for which scars will no longer become visible in the Husimi distribution. Another consequence of Eq. (5.3) is that if un-
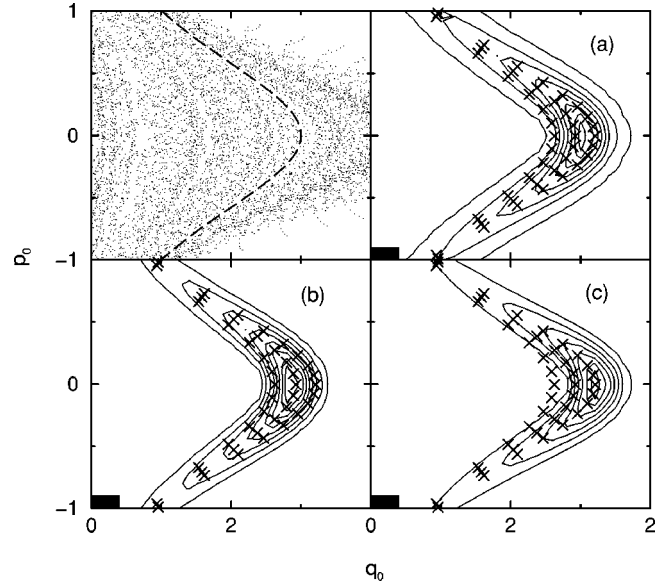

FIG. 16. Poincaré surface of section and Husimi distributions of three dominant Floquet states for the kicked $n_i = 50$ atom with $\Delta p_0 = 0.01$ and $\nu_0 = 16.8$. The figures are ordered according to the importance of the Floquet states in the time evolution. The dashed line in the surface of section represents the initial energy level of the system. Crosses are fixed points belonging to unstable periodic orbits with a period $15T$, $17T$, or $19T$.

stable periodic orbits of similar period have fixed points in close proximity to each other such that

$$\frac{1}{\sqrt{n_i}} \gtrsim \sqrt{(q_0^i - q_0^j)^2 + (p_0^i - p_0^j)^2}, \qquad (5.4)$$

the Husimi distribution can no longer resolve scars of individual periodic orbits. Several periodic orbits are then carriers of the localized quantum phase space distribution of an individual Floquet state. An example is shown in Fig. 16 for the kicked Rydberg atom with weak positive kicks. For this system, many periodic orbits with comparable periods which are equally likely to be excited lie close to the initial torus. In this case, fixed points are so densely distributed that several of them exist in the area corresponding to the quantum uncertainty $\Delta q_0 \Delta p_0 \simeq 1/n_i$ and contribute to the Husimi distribution of the dominant localized Floquet states. As n_i increases, the Husimi distribution can increasingly resolve different periodic orbits (Fig. 17). However, even at $n_i = 100$, the Husimi distribution still contains more than one periodic orbit. This picture of the (quasi) periodic motion of the quantum wave packet finds its direct verification in the time dependence of the survival probability. As shown in Fig. 6, the survival probability for the negatively kicked Rydberg atom displays oscillations with a period $9T$ which is precisely the period for upward and downward motion in energy along the periodic orbit. The fact that the orbit is classically unstable is borne out by the fact that the oscillation of the classical survival probability decays after about two periods ($\chi_{\text{PO}} \approx 0.5$). Conversely, the quantum oscillations in probability remain stable over hundreds of periods.
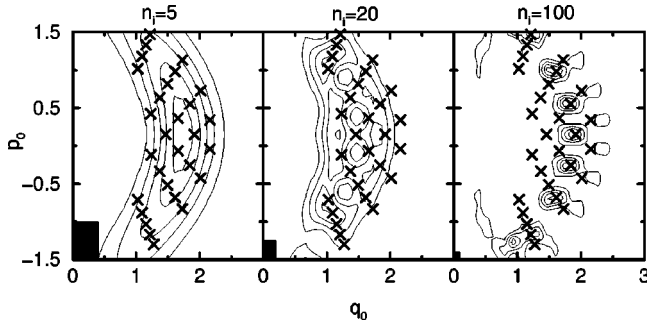
FIG. 17. Husimi distribution of a dominant Floquet state with different initial states: (a) $n_i=5$, (b) $n_i=20$, and (c) $n_i=100$. The parameters of the perturbation are the same as in Fig. 13.

In Fig. 14, we can observe that the wave packet evolves back and forth across the ionization threshold for the first few kicks. When it goes through the area which has densely distributed fixed points belonging to the different periodic orbits ($t \sim 5T$ in Fig. 14), the quantum wave packet "forgets" the original periodic orbit and becomes redistributed among different periodic orbits. Due to this redistribution, different parts of the wave packet start evolving with different periods of the motion. This dephasing creates an additional slow oscillation in the survival probability and the partial revival of the oscillation amplitude (Fig. 6).

The scars of unstable periodic orbits also leave a mark on the spectral distribution of quantum localization. This allows one to make a direct connection between scars, quantum localization, and the additional structures observed in the spectral distribution. Figure 18 is a magnification of the energy distribution for negative kicks (Fig. 10). The vertical lines denote the energetic positions of the classical unstable periodic orbits with period $7T$ [Fig. 18(a)], and $9T$ [Fig. 18(b)]. Obviously, the additional rapid variation of the energy distributed near the maximum represents the jumping from one fixed point to the next fixed point along the orbit. Note that the structures are not an artifact of the energy resolution of the discrete pseudostate basis. There are, typically, several
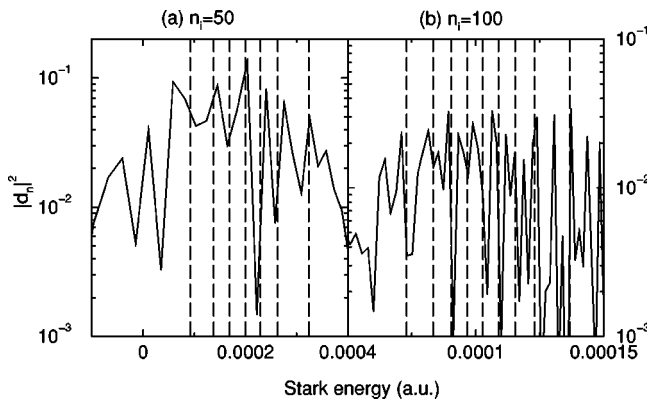

FIG. 18. Energy distributions of the Floquet states (solid line) and energy levels of the unstable fixed points (vertical dashed lines). The strength of the kicks is $\Delta p_0 = -0.3$ and the frequency is $\nu_0 = 16.8$. For $n_i = 50$. The unstable fixed points for $n_i = 50$ and $n_i = 100$ belong periodic orbits with period $7T$ and $9T$, respectively.

pseudostate energies within the peak. The fact that not all peaks are accounted for by the energetic positions of the fixed points is due to the fact that one Floquet state may contain scars from more than one periodic orbit.

The relation to the localization length follows from the width of the peaked structure. The peaks that are connected by a single periodic orbit have comparable height which is an obvious consequence of the fact that the probability for finding the wave packet at different fixed points along a given orbit varies only slightly. The width of the plateaulike substructure is therefore given by the maximum energy excursion along the orbit from $E_{\min}^{\text{Stark}}$ to $E_{\max}^{\text{Stark}}$,

$$\Delta E_{cl} = E_{\max}^{\text{Stark}} - E_{\min}^{\text{Stark}}. \tag{5.5}$$

Beyond this width, the spectral distribution is rapidly decaying. Comparing ΔE_{cl} with the localization length Δ_L in Fig. 10, we find

$$\langle \Delta E_{\text{cl}} \rangle \simeq \Delta_L, \tag{5.6}$$

i.e., the size of the quantum localization can be estimated from the energy excursion along classical periodic orbits. The average is taken over the ensemble of the periodic orbits which contribute to the scarring of the dominant Floquet states. We find Eq. (5.6) to hold for both negative and positive kicks over a wide range of kick strengths. The important implication is that a generic quantum property, the quantum localization length, can be estimated from purely classical information about scars.

VI. CONCLUSIONS AND OUTLOOK

We have demonstrated the existence of different mechanisms of quantum localization of the kicked Rydberg atom within a fully chaotic region in phase space. We have shown that the suppression of nonresonant diffusion results in a localization phenomenon resembling strong Anderson localization. We note, however, that a direct mapping of the Hamiltonian onto a tight-binding Anderson Hamiltonian has not been achieved. While the analytic steps taken for the mapping from the kicked rotor can be applied here as well, the intrinsic randomness of the "site energies" in the resulting tight-binding model has not been proven. Instead, in the present case we find that the quantum localization length is intimately related to the localization around classical unstable periodic orbits. Scars of unstable orbits are imprinted on the quantum phase space distributions of the dominant stable Floquet states. Remarkably, the quantum localization length can be estimated from the classical energy excursion along unstable periodic orbits. In addition, a different localization mechanism is operative suppressing resonant energy diffusion due to sequential "photon" absorption. This localization is nonexponential in energy space due to the fact that the high harmonics of the perturbation play asignificant role in the excitation dynamics. The latter is responsible for the

difference to the photonic localization for the microwave ionization problem [2,9].

While for this one-dimensional system a fairly complete understanding of the origin and properties of quantum localization has been achieved, the central open question is that of dimensionality. Anderson localization is known to be strongly dependent on the dimension of the system. It remains to be analyzed if and to what extent quantum localiza-

tion can be observed for the 3D Rydberg atom. We hope that the present work will stimulate high-frequency experiments for this problem.

[1] F. L. Moore, J. C. Robinson, C. F. Bharucha, B. Sundaram, and M. G. Raizen, Phys. Rev. Lett. **75**, 4598 (1995).

[2] P. Koch and K. Van Leeuwen, Phys. Rep. **255**, 290 (1995).

[3] C. O. Reinhold, J. Burgdörfer, M. T. Frey, and F. B. Dunning, Phys. Rev. Lett. **79**, 5226 (1997).

[4] M. T. Frey, F. B. Dunning, C. O. Reinhold, S. Yoshida, and J. Burgdörfer, Phys. Rev. A **59**, 1434 (1999).

[5] G. Casati B. V. Chirikov, F. M. Izraelev, and J. Ford, Lect. Notes. Phys. **93**, 334 (1997).

[6] P. W. Anderson, Phys. Rev. **109**, 1492 (1958).

[7] S. Fishman, D. R. Grempel, and R. E. Prange, Phys. Rev. Lett. **49**, 509 (1982).

[8] G. Casati, B. V. Chirikov, D. L. Shepelyansky, and I. Guarneri, Phys. Rep. **154**, 77 (1987).

[9] R. V. Jensen, S. M. Susskind, and M. M. Sanders, Phys. Rep. **201**, 1 (1991).

[10] C. O. Reinhold, M. Melles, H. Shao, and J. Burgdörfer, J. Phys. B **26**, L659 (1993).

[11] J. E. Bayfield, G. Casati, I. Guarneri, and D. W. Sokol, Phys. Rev. Lett. **63**, 364 (1989).

[12] M. Rotenberg, Adv. At. Mol. Phys. **6**, 233 (1970).

[13] S. Yoshida, C. O. Reinhold, J. Burgdörfer, B. E. Tannian, R. A. Poppole, and F. B. Dunning, Phys. Rev. A **58**, 2229 (1998).

[14] S. Yoshida, S. Watanabe, C. O. Reinhold, and J. Burgdörfer, Phys. Rev. A **60**, 1113 (1999).

[15] Dž Belkić, J. Phys. B **14**, 1907 (1981).

[16] I. Bersons and A. Kulsh, Phys. Rev. A **55**, 1674 (1997).

[17] J. H. Shirley, Phys. Rev. **138**, B979 (1965).

[18] S. Yoshida, C. O. Reinhold, P. Kritöfel, J. Burgdörfer, S. Watanabe, and F. B. Dunning, Phys. Rev. A **59**, R4121 (1999).

[19] C. F. Hillermeier, R. Blümel, and U. Smilansky, Phys. Rev. A **45**, 3486 (1992).

[20] K. Husimi, Proc. Phys. Math. Soc. Jpn. **22**, 264 (1940); M. Hillery, R. F. O'Connell, M. O. Scully, and E. P. Wigner, Phys. Rep. **106**, 121 (1984).

[21] E. Ott, *Chaos in Dynamical Systems* (Cambridge University Press, New York, 1993).

[22] B. Mirbach and H. J. Korsch, Ann. Phys. (N.Y.) **265**, 80 (1998).

[23] T. A. Brody, J. Flores, J. French, P. Mello, A. Pandey, and S. Wong, Rev. Mod. Phys. **53**, 3851 (1981).

[24] E. J. Heller, Phys. Rev. Lett. **53**, 1515 (1984).